Aharonov–Bohm interference of fractional quantum Hall edge modes

J. Nakamura[1,2], S. Fallahi[1,2], H. Sahasrabudhe [1], R. Rahman [3], S. Liang[1,2], G. C. Gardner[2,4] and M. J. Manfra [1,2,3,4,5]*

The braiding statistics of certain fractional quantum Hall states can be probed via interferometry of their edge states. Practical difficulties—including loss of phase coherence—make this a challenging task. We demonstrate the operation of a small Fabry–Perot interferometer in which highly coherent Aharonov–Bohm oscillations are observed in the integer and fractional quantum Hall regimes. Careful design of the heterostructure suppresses Coulomb effects and promotes strong phase coherence. We characterize the coherency of edge-mode interference by the energy scale for thermal damping and determine the velocities of the inner and outer edge modes independently via selective backscattering of edge modes originating in the $N = 0, 1, 2$ Landau levels. We also observe clear Aharonov–Bohm oscillations at fractional filling factors $\nu = 2/3$ and $\nu = 1/3$, which indicates that our device architecture provides a platform for measurement of anyonic braiding statistics.

nteger and fractional quantum Hall states are archetypal topological phases of a two-dimensional electron system (2DES) subjected to a strong perpendicular magnetic field[1]. Electronic Fabry–Perot interferometry has been proposed as a means to probe the properties of integer and fractional quantum Hall edge states[2–5]; most intriguingly, interferometry may be used to directly observe anyonic braiding statistics[6] of fractional quantum Hall quasiparticles. Interference visibility in real devices is limited by finite phase coherence, a particularly acute problem in the fractional quantum Hall regime. Visibility may be improved by decreasing the size of the interferometer so that the path travelled by interfering excitations is shorter. However, attempts to measure interference in small devices have yielded results inconsistent with simple Aharonov–Bohm interference; specifically, the magnetic field oscillation period is found to change with filling factor, and constant phase lines in the gate voltage–magnetic field plane have positive slope rather than the expected negative slope[7–10]. This behaviour was attributed to Coulomb charging effects[11,12], which cause the area of the interferometer to change as the magnetic field is varied. This 'Coulomb-dominated' behaviour masks the Aharonov–Bohm phase and makes braiding statistics unobservable[12]. The effects of intermediate Coulomb coupling were also investigated theoretically[13]. The challenge for measuring robust interference and observing fractional braiding statistics is to create a device small enough to maintain phase coherence, while reducing Coulomb effects so that the device may operate in the Aharonov–Bohm regime. We report fabrication and operation of an interferometer that overcomes these challenges.
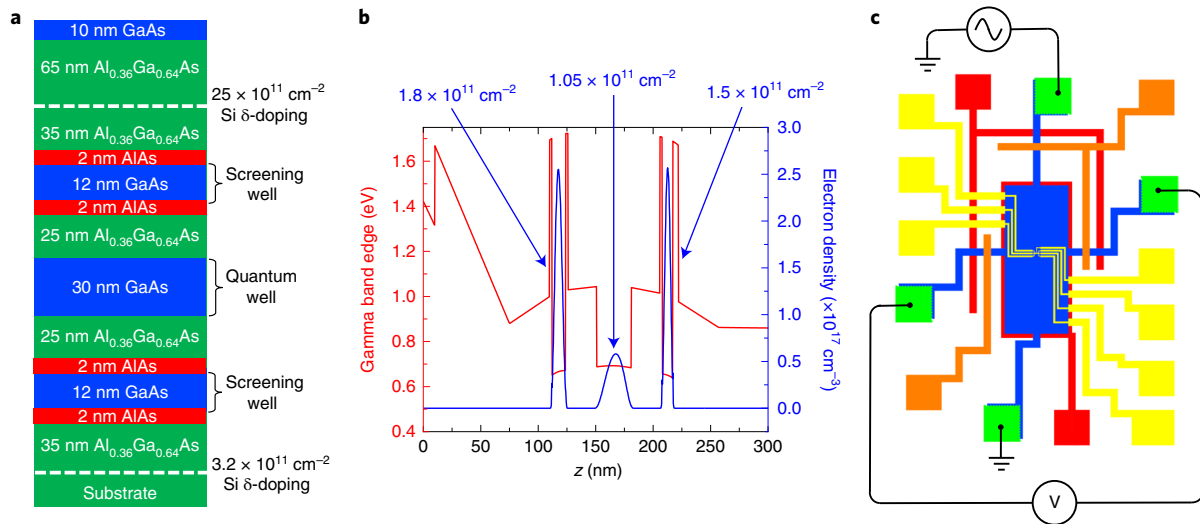
We grew the GaAs/AlGaAs heterostructure by molecular beam epitaxy[14,15] and it is shown in Fig. 1a. While typical structures utilize a single GaAs quantum well in which the 2DES resides, our structure contains three GaAs wells: a primary quantum well 30 nm wide and two additional 12 nm wells located on either side of the primary well separated by 25 nm $Al_{0.36}Ga_{0.64}As$ spacers. The 2DES under study is located inside the primary GaAs quantum well, while the ancillary wells screen Coulomb effects so that the interferometer may operate in the Aharonov–Bohm regime[11,12]. The structure

is modulation doped with silicon above the top screening well and below the bottom screening well. In Fig. 1b we show the position of the Γ-band edge (red) and electron density (blue) calculated by the self-consistent Schrodinger–Poisson method[16]; the confinement energy in each screening well is tuned to match the experimentally measured densities. This structure is designed to have significantly higher density in the screening wells than in the primary well to facilitate strong screening.
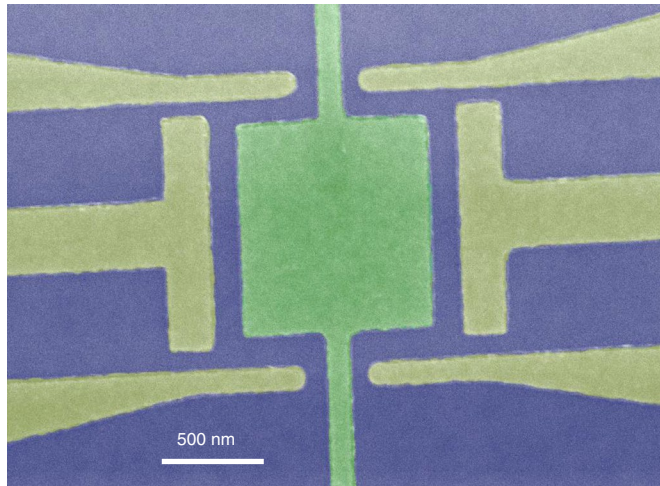
In Fig. 2 we show a scanning electron micrograph of the interferometer gates. The device consists of two quantum point contacts (QPCs) that form narrow constrictions and a pair of side gates that define the interference path. The gates shown in yellow are negatively biased to deplete electrons from the quantum well and define the interference path; the central top gate (green) is grounded and does not alter the 2DES density.

Interferometer operation requires transport measurements through the primary quantum well unobscured by parallel conduction through the screening wells. Our device includes narrow gates on the top surface and on the back side of the chip that partially overlay the arms connecting each Ohmic contact to the mesa; this is shown schematically in Fig. 1c. The surface gates over the Ohmics are negatively biased at −0.29 V; this bias is sufficient to deplete the electrons from the top screening well without depleting either the primary quantum well or the bottom screening well. Similarly, the back-side gate over the Ohmics is biased at −150 V to deplete the bottom screening well, but not the primary quantum well. This eliminates electrical conduction through both screening wells so that only the primary quantum well is probed in measurements. As these gates are well separated from the gates that define the mesoscopic interference path, the screening wells are still populated in the interferometer and thus available to screen. In Fig. 3a we show the evolution of the Hall resistance R_{xy} with current allowed to flow through all three wells (black trace), with the top screening well disconnected from the contacts (blue trace), and with both screening wells disconnected such that current passes only through the primary quantum well (red trace); in the final case, R_{xy} exhibits a much

[1]Department of Physics and Astronomy, Purdue University, West Lafayette, IN, USA. [2]Birck Nanotechnology Center, Purdue University, West Lafayette, IN, USA. [3]School of Electrical and Computer Engineering, Purdue University, West Lafayette, IN, USA. [4]Microsoft Station Q Purdue, Purdue University, West Lafayette, IN, USA. [5]School of Materials Engineering, Purdue University, West Lafayette, IN, USA. *e-mail: mmanfra@purdue.edu

Fig. 1 | Heterostructure design and device layout. a, Layer stack of the GaAs/AlGaAs heterostructure along the growth direction, showing the positions of the GaAs quantum well and screening wells (blue), AlGaAs spacers (green) and AlAs barriers (red). **b**, Conduction band edge (red) and electron density (blue) versus growth direction (z axis) calculated using a self-consistent Schrodinger–Poisson method. The sheet density in each well is indicated. **c**, Schematic showing the layout of the mesa (blue), Ohmic contacts (green), surface gates used to isolate the top screening well from the contacts (orange) and the backgate used to isolate the contacts from the bottom screening well (red). The surface gates used to define the interference path are shown in yellow. Additionally, there is a global backgate underneath the mesa (red). A four-terminal measurement circuit is indicated in which current is injected into the Hall bar and the perpendicular Hall voltage is measured; when the interferometer gates are biased to define the interference path, the measured resistance is referred to as the diagonal resistance, R_D.


Fig. 2 | Scanning electron micrograph of the interferometer. False-colour scanning electron micrograph of the interferometer, located in the centre of the Hall bar shown schematically in Fig. 1c. The device consists of two QPCs to backscatter current and a pair of side gates to define the interference path (yellow); when these gates are negatively biased, the 2DES underneath is depleted, which defines the interference path. In the measurements, the gate voltage V_gate applied to both side gates is varied to change the area of the interference path. An additional gate over the top of the area of the device (green) is grounded for these experiments.

steeper slope and shows clear quantum Hall plateaus and concomitant zeros in longitudinal resistance (not shown), demonstrating that parallel conduction through the screening wells has been eliminated. This selective depletion technique was pioneered to isolate transport in bulk bilayer systems[17]. Here we have demonstrated that the technique has utility for mesoscale electronic devices as well.

The presence of the screening wells acts to reduce the Coulomb charging energy, characterized by measuring Coulomb blockade through the device at zero magnetic field[18]. Coulomb blockade diamonds (obtained by measuring the differential conductance $\frac{\partial I}{\partial V}$ versus side-gate voltage V_gate and source–drain voltage V_SD), shown in Fig. 2b, yield a charging energy $\frac{e^2}{2C} \approx 17\,\mu\mathrm{eV}$. The Coulomb blockade charging energy characterizes the incremental increase of electrostatic energy when an electron is added in the presence of all the other electrons localized in the interior of the device; therefore, this energy may be loosely identified with the bulk–edge coupling constant K_IL in ref. [12], which determines whether the device is in the Coulomb-dominated or Aharonov–Bohm regime. A similarly sized device without screening wells would have charging energy $\frac{e^2}{2C} \sim \frac{e^2}{er} \approx 200\,\mu\mathrm{eV}$ (where r is the radius of the dot), indicating that the screening wells are very effective at reducing Coulomb effects in the interferometer (Coulomb blockade from a device without screening wells is shown in Supplementary Fig. 1). It is important to note that although Coulomb effects are screened on the scale of the mesoscopic device, the presence of several fractional quantum Hall plateaus visible in Fig. 3a indicates that the Coulomb interaction on the microscopic length scales relevant for the fractional quantum Hall effect is not significantly reduced.

$\nu = 1$ interference

Next, we operate the device at filling factor $\nu = 1$ in the integer quantum Hall regime, where the bulk of the 2DES is insulating and current is carried by a chiral edge state. The interference path is shown schematically in Fig. 4a. Electrons incident from the source contact are backscattered by the two QPCs to the opposite edge, and the two backscattered paths interfere; this is shown schematically in Fig. 4a. The quantum mechanical phase difference between the two interfering paths is given by the Aharonov–Bohm phase: $\theta = 2\pi \frac{A_\mathrm{I} B}{\Phi_0}$, where A_I is the area of the interference path, B is the magnetic field and $\Phi_0 \equiv \frac{h}{e}$ is the magnetic flux quantum. The device may be operated by changing the magnetic field B, or by changing the voltage on the side gates to change A_I.
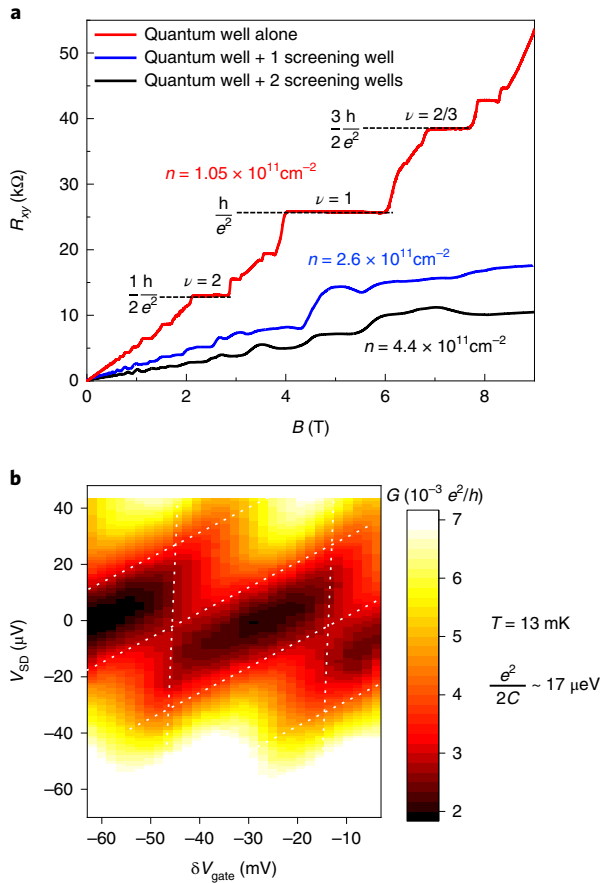
Fig. 3 | Bulk magnetotransport and Coulomb blockade. a, Bulk Hall conductance R_{xy} with the top and bottom gates around the contacts grounded (black trace), with -0.29 V on the top gate to disconnect the top screening well from the contacts (blue), and with -0.29 V on the top gate and -150 V on the backgate around the contacts to disconnect both screening wells from the contacts so that transport is only measured through the primary quantum well (red). The red trace is taken at temperature $T = 13$ mK, and the blue and black traces are taken at $T = 300$ mK. Magnetotransport across the device is shown in Supplementary Fig. 2. **b**, Coulomb blockade measurement at zero magnetic field measured in a dilution refrigerator at base temperature $T = 13$ mK showing the differential conductance $\frac{\partial I}{\partial V}$ versus gate voltage and source–drain voltage V_{SD} for the device at zero field showing Coulomb blockade diamonds with charging energy $\frac{e^2}{2C} \approx 17$ μeV. δV_{gate} is relative to -1.8 V.

At $\nu = 1$ the interferometer exhibits strong conductance oscillations, probed by measuring the diagonal resistance R_D across the device. R_D as a function of gate voltage and magnetic field is plotted in Fig. 4b; the lines of constant phase exhibit negative slope, consistent with the device being in the Aharonov–Bohm regime despite its small size. The magnetic field oscillation period $\Delta B = 5.7$ mT, which gives an area of the interference path $A_I = \Delta B/\Phi_0 \approx 0.73$ μm². This area is smaller than the lithographic area of the device, indicating that the 2DES is depleted in a region approximately 180 nm wide around the gates; this agrees with simulations of the 2DES density at the edge of the gate (see Supplementary Fig. 3). Additionally, we find that ΔB does not vary significantly with filling factor in the range $1 \leq \nu \leq 12$, consistent with Aharonov–Bohm behaviour and in contrast to the Coulomb-dominated regime in which ΔB is proportional to $1/\nu$ (refs. [7,10–12]). Previous Fabry–Perot interferometry experiments utilizing conventional heterostructures have required a device area of 20 μm² for Coulomb effects to be small enough for

the device to be in the Aharonov–Bohm regime[7,10]; unambiguous observation of the Aharonov–Bohm regime in a much smaller device demonstrates the effectiveness of the device design employed here.

For weak backscattering by symmetrically tuned QPCs, conductance oscillations due to interference obey $G / G_0 = 1 - 2r^2\left[1 + \eta \cos\left(2\pi\frac{AB}{\Phi_0}\right)\right]$, where $G = \frac{1}{R_D}$ is the conductance across the device, $G_0 \equiv \frac{e^2}{h}$ is the conductance quantum, r^2 is the reflection probability of the QPCs and η is the coherence factor. We characterize coherence of the interference at $\nu = 1$ by measuring conductance oscillations at different cryostat temperatures, plotted in Fig. 4c; we normalize by dividing the conductance oscillations δG by the reflection amplitude r^2, with each QPC tuned to approximately 97% transmission and 3% reflection. The coherence factor η (defined as the amplitude of $\frac{\delta G}{2G_0 r^2}$) decays with temperature following an approximately exponential trend, shown in Fig. 4d, with a characteristic temperature $T_0 = 206$ mK. For comparison, in measurements of a Fabry–Perot interferometer in ref. [19], T_0 was found to be less than 20 mK for magnetic fields exceeding 1.5 T; in measurements of Mach–Zehnder interferometers the largest T_0 measured was 40 mK (ref. [20]), with larger devices exhibiting smaller T_0. The significantly larger T_0 observed in our experiment indicates that the smaller size achieved in our device is beneficial to achieving quantum coherence.

Edge-mode velocity

When the device is operated at a lower magnetic field (higher filling factor), multiple integer edge modes are present. In our device it is possible to selectively interfere a particular edge mode by tuning the QPC voltages to partially backscatter that edge, while fully transmitting the outer edges so that only the partially backscattered edge interferes; this is shown schematically in Fig. 5a for the case of bulk filling factor $\nu_{bulk} = 3$, and a corresponding trace of the QPC conductance versus gate voltage is shown in Fig. 5b with the operating points corresponding to the selective interference of each edge mode indicated with coloured circles.

The interference phase may be additionally modulated by changing the energy ϵ of injected electrons, which changes the wavevector k. This introduces a phase shift $\delta\theta = \delta\epsilon\frac{\partial k}{\partial \epsilon}L = \frac{\delta\epsilon L}{\hbar v_{edge}}$, where L is the path length around the interference loop and $v_{edge} \equiv \frac{1}{\hbar}\frac{\partial \epsilon}{\partial k}$ is the velocity of the edge mode[2]. ϵ may be modulated by applying a finite source–drain bias V_{SD} across the device; this results in oscillations in differential conductance as a function of both V_{SD} and flux: $\delta G \propto \cos\left(2\pi\frac{AB}{\Phi_0}\right)\cos\left(\frac{eV_{SD}L}{2\hbar v_{edge}}\right)$ (ref. [21]). This results in nodes in a 'chequerboard' pattern when δG is measured in the $V_{SD} - V_{gate}$ plane (plotted at $\nu_{bulk} = 1$ in Fig. 5c and for the inner $N = 1$ mode at $\nu_{bulk} = 3$ in Fig. 5d), with nodes in the interference pattern occurring at $V_{SD} = \pm\frac{\pi\hbar v_{edge}}{eL}$. The velocity may thus be extracted: $v_{edge} = \frac{eL\Delta V_{SD}}{2\pi\hbar}$ (refs. [21,22]), where ΔV_{SD} is the spacing between nodes, and we estimate L from the interference area, $L \approx 4\sqrt{A_I}$. The extracted velocity probably represents the average velocity of the edge mode in the interferometer since there may be local variations in the confining potential and thus velocity.

In ref. [21] this method was used to measure edge velocity versus filling factor, but without controlling which edge mode was being interfered; in ref. [22] edge velocity for only the $N = 0$ Landau level was reported (where $N = 0, 1, 2\ldots$ is the Landau level index). In Fig. 5e we plot the edge-state velocity for the $N = 0$, $N = 1$ and $N = 2$ Landau level edge modes versus bulk filling factor ν_{bulk}. The inner, higher-index Landau levels generally have lower velocity and correspondingly lower coherence. At magnetic fields below approximately 1.2 T ($\nu_{bulk} = 4$), the QPCs show spin-degenerate conductance plateaus,
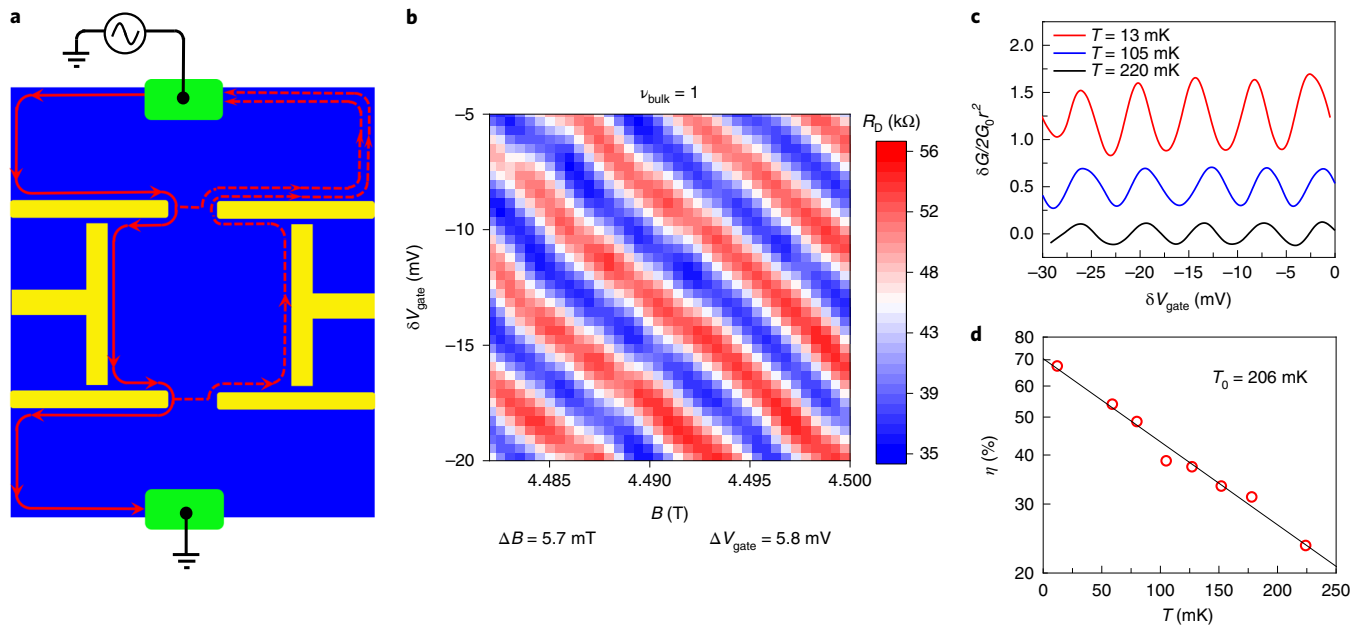
Fig. 4 | Interference measurements at $\nu = 1$. a, Schematic showing the interference path defined by the interferometer gates at $\nu = 1$. **b**, Resistance oscillations as a function of magnetic field B and side-gate voltage δV_{gate} (relative to -1.4 V) showing clear Aharonov–Bohm interference. For this measurement the QPCs are biased to achieve approximately 25% reflection. **c**, Oscillations in conductance through the device, δG, divided by the QPC backscattering amplitude, r^2, at 13 mK (red), 105 mK (blue) and 220 mK (black). For these measurements each QPC is tuned to approximately 97% transmission and 3% reflection ($r^2 = 0.03$). The amplitude of the oscillations clearly decreases as the cryostat temperature is increased. **d**, Coherence factor η versus temperature; η shows an approximately exponential dependence on temperature with a characteristic decay scale of 206 mK.

even though the bulk transport exhibits spin-split quantum Hall states down to 0.2 T. This suggests that although distinct edge states exist, below 1.2 T they are too close to one another to be interfered independently; therefore, at filling factors $\nu_{bulk} > 4$ we show a single velocity measurement for each Landau level, while at lower fillings we show both spins when resolved. We also mention that we observe the same period-halving phenomenon in our device that was reported in previous interferometry experiments[23–25] (see Supplementary Section 2 and Supplementary Fig. 4).

Much of the magnetic field dependence in Fig. 5e can be understood from the fact that edge currents in the quantum Hall regime are generated by Hall drift: $\mathbf{v}_{Hall} = \frac{\mathbf{E} \times \mathbf{B}}{B^2}$, where $\mathbf{E}$ is the in-plane electric field at the edge due to the confining potential and $\mathbf{B}$ is the perpendicular magnetic field. This implies that the edge velocity should increase with decreasing magnetic field (increasing filling factor), and this is indeed the predominant trend observed at filling factors $2 < \nu_{bulk} < 9$. On the other hand, it must also be considered that the electric field experienced by each edge state also depends on both magnetic field and Landau level index. We see in Fig. 5e that the outer, lower-index Landau levels generally have higher edge velocity than the inner, higher-index ones. This behaviour can be understood from the works of Chklovskii et al.[26,27], who found that the confining potential is steepest at the outer edge, resulting in a higher electric field and thus higher velocity for the outer Landau level edge modes and a smaller electric field and lower velocity for the inner ones.

The results of numerical simulations of edge transport in the integer quantum Hall regime for the heterostructure used in these experiments are plotted in Fig. 5f; see Supplementary Section 3 and ref. [16] for an in-depth review. In these simulations, the spatially varying in-plane electric field is self-consistently evaluated for the Landau level density of states, considering the electrostatic effects of the heterostructure, doping, surface states and gates. We obtain the velocity by solving quantum transport (non-equilibrium Green's function) equations at the Fermi level.

The simulations show good qualitative and quantitative agreement with the experimental results over the range of filling factor $2 < \nu_{bulk} < 10$. At lower filling $\nu_{bulk} < 2$, the edge velocity exhibits non-monotonic behaviour. This behaviour may be due to the impact of electron–electron interactions, which become increasingly important at high magnetic field. Non-monotonic behaviour at low filling was also reported in ref. [22]. Our simulations employ a mean-field Hartree approximation that does not capture many-body effects.

Additionally, the edge velocities also exhibit non-monotonic behaviour at high filling $\nu_{bulk} > 10$. A possible explanation for this is that at low fields when the magnetic length becomes comparable to the length scale of the confining potential at the edge, charge transport may occur via skipping orbits, resulting in different behaviour than observed at higher fields[21,28]. It is reasonable for this to occur at $\nu_{bulk} = 10$; here the magnetic length is approximately 39 nm, and simulations indicate that the length scale of the confining potential is approximately 40 nm (see Supplementary Fig. 3). This effect is not captured in the simulations as the magnetic length approaches the Debye length. An alternative possibility is that at high filling where the cyclotron gap is smaller, there may be partial equilibration between the edge modes facilitated by the applied V_{SD}, which would make our assumption of interfering a single edge mode invalid.

Fractional quantum Hall regime

We turn now to results in the fractional quantum Hall regime. In previous experiments with small Fabry–Perot devices Coulomb-dominated or Coulomb blockade oscillations have been observed in fractional states[10,29–31]. Willet et al.[32,33] reported oscillations at $\nu = 5/2$ consistent with Aharonov–Bohm interference of charge $e/4$ and $e/2$ excitations. However, oscillations with negatively sloped lines of constant phase in the gate voltage–magnetic field plane (a distinctive sign of Aharonov–Bohm regime interference) have not been previously reported. Edge modes in the fractional quantum Hall regime are predicted to have remarkably different properties
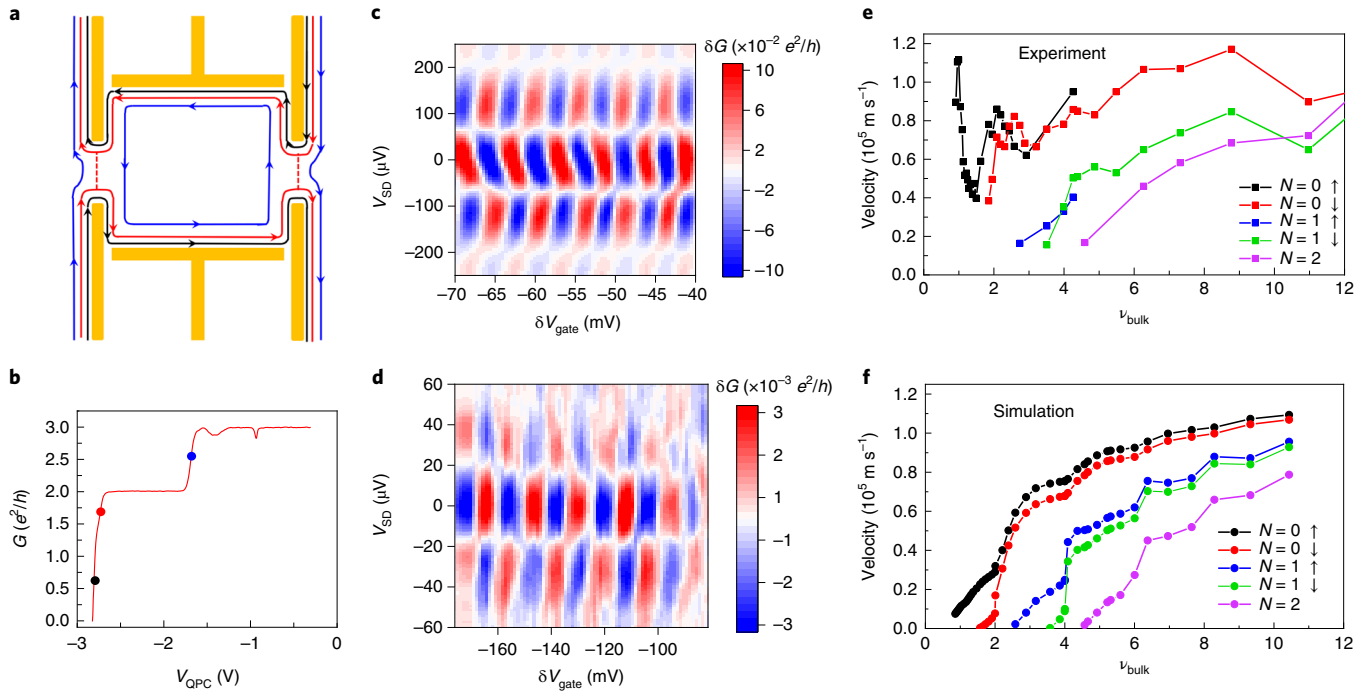
Fig. 5 | Edge-mode velocity measurements. a, Schematic showing an interference path with multiple edge states in which the outermost mode is fully transmitted, the innermost mode is fully backscattered by both QPCs and the middle mode is partially transmitted by both QPCs; in this configuration only the middle mode is interfered. **b**, Conductance versus gate voltage for one QPC at $B = 1.64\,\text{T}$ and $\nu_{\text{bulk}} = 3$ with other interferometer gates grounded. The blue, red and black circles indicate the operating point for interference of the modes associated with $\nu = 3$, $\nu = 2$ and $\nu = 1$, respectively. **c,d**, Differential conductance at $\nu_{\text{bulk}} = 1$ interfering the $\nu = 1$ mode (**c**) and at $\nu_{\text{bulk}} = 3$ interfering the innermost $\nu = 3$ mode (**d**) as a function of side-gate voltage and source–drain voltage. δV_{gate} is relative to $-1.4\,\text{V}$. **e**, Edge-state velocity extracted from the differential conductance oscillations for different edge modes as a function of bulk filling factor. At magnetic fields below approximately 1.2 T (bulk filling factor $\nu = 4$) conductance through the QPCs is no longer spin-resolved, so only a single line is displayed for each Landau level. Experimental uncertainty is estimated at $\pm 13\%$; see Supplementary Section 1. **f**, Numerically calculated edge-state velocities for the $N = 0, 1$ and 2 Landau levels.

from those in the integer states; in particular, the current-carrying quasiparticles may carry fractional charge. In the fractional case, the Aharonov–Bohm interference phase is modified[12]:

$$\theta = 2\pi \frac{e^{\star}}{e} \frac{A_{\text{I}} B}{\Phi_0} \tag{1}$$

As long as the QPCs are not pinched off, the edge modes and the electrons forming the fractional quantum Hall condensate are not localized within the interferometer, so the area A_{I} should change continuously as the gate voltage is varied. Equation (1) indicates that quasiparticle charge may be extracted from gate-voltage oscillation periods according to the relationship $\frac{e^{\star}}{e} = \frac{\Phi_0}{B \Delta V_{\text{gate}} \frac{\partial A_{\text{I}}}{\partial V_{\text{gate}}}}$, where ΔV_{gate} is the gate-voltage oscillation period and $\frac{\partial A_{\text{I}}}{\partial V_{\text{gate}}}$ is the lever arm relating change in gate voltage to the change in interference path area. $\frac{\partial A_{\text{I}}}{\partial V_{\text{gate}}}$ may be determined from the gate-voltage period at integer states, where the interfering charge is simply e; a linear fit of ΔV_{gate} versus $1/B$ yields $\frac{\partial A_{\text{I}}}{\partial V_{\text{gate}}} = 1.8 \times 10^{-13}\,\text{m}^2\,\text{V}^{-1}$ (gate and magnetic field periods are shown in Supplementary Fig. 5 and discussed in Supplementary Section 4).

In both the Laughlin[34] and composite fermion[1,35] theories, the $\nu = 1/3$ fractional quantum Hall effect state is predicted to support quasiparticles with charge $e^{\star} = e/3$. At $\nu = 1/3$ ($B = 13\,\text{T}$), we observe conductance oscillations as a function of gate voltage and magnetic field similar to those at integer states; the oscillations have

gate-voltage period $\Delta V_{\text{gate}} = 6.1\,\text{mV}$; this yields an interfering quasiparticle charge $e^{\star} = e \frac{\Phi_0}{B \Delta V_{\text{gate}} \frac{\partial A_{\text{I}}}{\partial V_{\text{gate}}}} = 0.29e$, in good agreement with the theoretical predictions. The oscillations at $\nu = 1/3$ are plotted in Fig. 6a. This supports previous experimental results utilizing shot noise[36], resonant tunnelling[37,38] and Coulomb blockade[29]. We mention that interference at $\nu_{\text{bulk}} = 1/3$ was found to be reproducible using a range of different gate voltages as well as after thermally cycling the device to room temperature (see Supplementary Section 5 and Supplementary Fig. 6). QPC conductance at fractional states is shown in Supplementary Fig. 7.

Next we discuss the $\nu = 2/3$ fractional quantum Hall effect state, which is the hole-conjugate state to $\nu = 1/3$ (ref. [39]). Several edge structures have been proposed for the $\nu = 2/3$ state. Motivated by a picture in which the $\nu = 2/3$ consists of a $\nu = 1/3$ hole state imposed on a $\nu = 1$ background, MacDonald proposed that the $\nu = 2/3$ edge should consist of an inner edge mode of charge $e^{\star} = -e/3$ and an outer edge with $e^{\star} = e$ (ref. [40]). Chang[41] and Beenakker[42] constructed models consisting of two $e^{\star} = e/3$ edge modes; a later work indicated that a transition from the MacDonald edge structure to the Chang–Beenakker edge structure should occur as the confining potential is tuned from sharp confinement to soft confinement[43]. Yet another edge model was proposed by Kane et al. in which the presence of disorder leads to a single $e^{\star} = 2e/3$ charged edge mode and a counter-propagating neutral mode[44].

We measure conductance oscillations at $\nu = 2/3$ ($B = 6.8\,\text{T}$) with $\Delta V_{\text{gate}} = 3.7\,\text{mV}$, yielding a quasiparticle charge $e^{\star} = e \frac{\Phi_0}{B \Delta V_{\text{gate}} \frac{\partial A_{\text{I}}}{\partial V_{\text{gate}}}} = 0.93e$, which suggests interference of an integrally
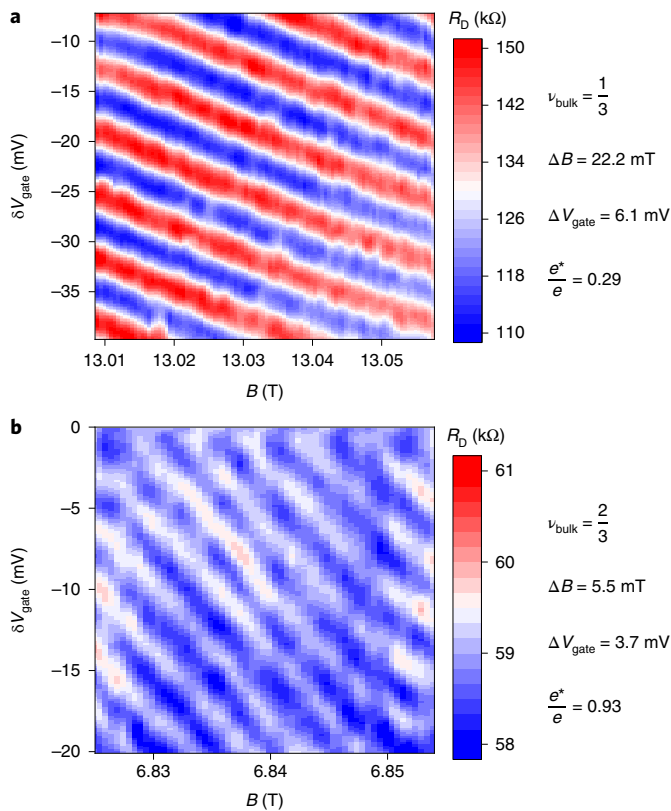
Fig. 6 | Interference of fractional quantum Hall states. a, Aharonov–Bohm conductance oscillations at $\nu = 1/3$. The QPCs are biased to approximately 22% reflection. **b**, Aharonov–Bohm conductance oscillations at $\nu = 2/3$. The QPCs are biased to approximately 20% reflection. In both cases, δV_{gate} is relative to −1.4 V.

charged edge mode. The oscillations at $\nu = 2/3$ are plotted in Fig. 6b. These oscillations have notably lower amplitude than those at both integer states and at $\nu = 1/3$ (see Supplementary Section 6 for a discussion of amplitudes). The presence of an integrally charged mode suggests that the Macdonald edge structure holds in our device. However, we do not find evidence for interference of a fractionally charged $e^* = -e/3$ mode at $\nu = 2/3$, even if the QPC bias is tuned to reduce backscattering. A possible explanation for this is that $e^* = -e/3$ should have a significantly smaller velocity due to being an inner mode; therefore, it will have lower phase coherence, making it very difficult to observe. Smaller device size or lower experimental temperatures might make measurement of the $-e/3$ mode possible.

It is noteworthy that our observation of an integrally charged mode differs from previous experimental findings, in which shot noise and Coulomb blockade measurements suggested a different edge structure consisting of two $e^* = e/3$ charge modes and two neutral modes[45,46], with no integrally charged mode observed. A possible explanation for this discrepancy is that our sample may have a sharper confining potential due to the short setback of the screening wells (see Supplementary Section 7 and Supplementary Fig. 8), resulting in our device supporting the edge structure described in ref. [40]. Our work provides evidence that experimental details such as the confining potential affect which of the candidate edge structures is formed at $\nu = 2/3$. We mention that a sharp confining potential may also be beneficial for measuring interference at the $\nu = 1/3$ state by preventing edge reconstruction and the proliferation of neutral edge modes[47–49] that may cause dephasing[50,51]; neutral modes have been detected at $\nu = 1/3$ and numerous other fractional quantum Hall states in standard GaAs structures without screening wells[52].

Finally, we remark that although we have observed Aharonov–Bohm interference of fractionally charged quasiparticles at the $\nu = 1/3$ fractional quantum Hall state, we have not observed the fractional braiding statistics predicted for these quasiparticles[1,6]. It has been suggested that increasing the flux through the interferometer by one flux quantum should result in the addition of one quasiparticle into the area of the device to keep the system charge neutral; this should result in an interference phase jump $\Delta\theta_{anyon} = 4\pi/3$ at the $\nu = 1/3$ state[2,12]. We appear to measure only the Aharonov–Bohm phase when magnetic field is varied, suggesting that adding flux does not introduce quasiparticles in our device. Critically, the $\nu = 1/3$ state has a large energy gap for the creation of quasiparticles measured to be approximately 700 μeV in a 2DES of similar density[53]. This energy is more than an order of magnitude larger than the measured charging energy in our device $\left(\frac{e^2}{2C} \approx 17 \text{ μV}\right)$,

which suggests that when the magnetic field is varied it may be energetically favourable for the primary quantum well to remain at a fixed filling factor (without creating quasiparticles) rather than a fixed sheet density, with the energy cost of the variations in quantum well density reduced by the screening wells. When the experiment is performed at a fixed filling factor it is expected that only the Aharonov–Bohm phase of the quasiparticles will be observed when magnetic field and side-gate voltage are varied[2,4], consistent with our observations. An alternative method to introduce quasiparticles and measure braiding statistics would be to directly manipulate the electrostatic potential with a gate in the centre of the interferometer[2,4]; efforts are underway to fabricate devices with this type of gate.

Online content

Any methods, additional references, Nature Research reporting summaries, source data, statements of data availability and associated accession codes are available at https://doi.org/10.1038/s41567-019-0441-8.

References

1. Jain, J. K. *Composite Fermions* (Cambridge Univ. Press, Cambridge, 2007).
2. Chamon, C. et al. Two point-contact interferometer for quantum Hall systems. *Phys. Rev. B* **55**, 2331–2343 (1997).
3. Sarma, S. D., Freedman, M. & Nayak, C. Topologically protected qubits from a possible non-Abelian fractional quantum Hall state. *Phys. Rev. Lett.* **94**, 166802 (2005).
4. Stern, A. & Halperin, B. I. Proposed experiments to probe the non-Abelian $\nu = 5/2$ quantum Hall state. *Phys. Rev. Lett.* **96**, 016802 (2006).
5. Kim, E. Aharonov–Bohm interference and fractional statistics in a quantum Hall interferometer. *Phys. Rev. Lett.* **97**, 216404 (2006).
6. Halperin, B. I. Statistics of quasiparticles and the hierarchy of fractional quantized Hall states. *Phys. Rev. Lett.* **52**, 1583–1586 (1984).
7. Zhang, Y. et al. Distinct signatures for Coulomb blockade and interference in electronic Fabry–Perot interferometers. *Phys. Rev. B* **79**, 241304(R) (2009).
8. Lin, P. V., Camino, F. E. & Goldman, V. J. Electron interferometry in the quantum Hall regime: Aharonov–Bohm effect of interacting electrons. *Phys. Rev. B* **80**, 125310 (2009).
9. Baer, S. et al. Cyclic depopulation of edge states in a large quantum dot. *New J. Phys.* **15**, 023035 (2013).
10. Ofek, N. et al. Role of interactions in an electron Fabry–Perot interferometer operating in the quantum Hall effect regime. *Proc. Natl Acad. Sci. USA* **107**, 5276–5281 (2010).
11. Halperin, B. I. & Rosenow, B. Influence of interactions on flux and back-gate period of quantum Hall interferometers. *Phys. Rev. Lett.* **98**, 106801 (2007).
12. Halperin, B. I., Stern, A., Neder, I. & Rosenow, B. Theory of the Fabry–Perot quantum Hall interferometer. *Phys. Rev. B* **83**, 155440 (2011).
13. von Keyserlingk, C. W., Simon, S. H. & Rosenow, B. Enhanced bulk–edge Coulomb coupling in fractional Fabry–Perot interferometers. *Phys. Rev. Lett.* **115**, 126807 (2015).
14. Manfra, M. J. Molecular beam epitaxy of ultra-high-quality AlGaAs/GaAs heterostructures: enabling physics in low-dimensional electronic systems. *Annu. Rev. Condens. Matter Phys.* **5**, 347–373 (2014).

15. Gardner, G. C., Fallahi, S., Watson, J. D. & Manfra, M. J. Modified MBE hardware and techniques and role of gallium purity for attainment of two dimensional electron gas mobility >35 × 10⁶ cm²/Vs in AlGaAs/GaAs quantum wells grown by MBE. *J. Cryst. Growth* **441**, 71–77 (2016).

16. Sahasrabudhe, H. et al. Optimization of edge state velocity in the integer quantum Hall regime. *Phys. Rev. B* **97**, 085302 (2018).

17. Eisenstein, J. P., Pfeiffer, L. N. & West, K. W. Independently contacted two-dimensional electron systems in double quantum wells. *Appl. Phys. Lett.* **57**, 2324–2326 (1990).

18. Beenakker, C. W. J. Theory of Coulomb-blockade oscillations in the conductance of a quantum dot. *Phys. Rev. B* **44**, 1646–1656 (1991).

19. McClure, D. T. *Interferometer based studies of quantum Hall phenomena*. PhD thesis, Harvard Univ. (2012).

20. Roulleau, P. et al. Direct measurement of the coherence length of edge states in the integer quantum Hall regime. *Phys. Rev. Lett.* **100**, 126802 (2008).

21. McClure, D. T. et al. Edge-state velocity and coherence in a quantum Hall Fabry–Perot interferometer. *Phys. Rev. Lett.* **103**, 206806 (2009).

22. Gurman, I., Sabo, R., Heiblum, M., Umansky, V. & Mahalu, D. Dephasing of an electronic two-path interferometer. *Phys. Rev. B* **93**, 121412 (R) (2016).

23. Choi, H. K. et al. Robust electron pairing in the integer quantum Hall effect. *Nat. Commun.* **6**, 7435 (2015).

24. Sivan, I. et al. Interaction-induced interference in the integer quantum Hall effect. *Phys. Rev. B* **97**, 125405 (2018).

25. Frigeri, G. A., Scherer, D. D. & Rosenow, B. Subperiods and apparent pairing in integer quantum Hall interferometers. Preprint at https://arxiv.org/abs/1709.04504 (2017).

26. Chklovskii, D. B., Shklovskii, B. I. & Glazman, L. I. Electrostatics of edge channels. *Phys. Rev. B* **46**, 4026–4034 (1992).

27. Chklovskii, D. B., Matveev, K. A. & Shklovskii, B. I. Ballistic conductance of interacting electrons in the quantum Hall regime. *Phys. Rev. B* **47**, 12605–12617 (1993).

28. Montambaux, G. Semiclassical quantization of skipping orbits. *Eur. Phys. J. B* **79**, 215–224 (2011).

29. McClure, D. T., Chang, W., Marcus, C. M., Pfeiffer, L. N. & West, K. W. Fabry–Perot interferometry with fractional charges. *Phys. Rev. Lett.* **108**, 256804 (2012).

30. Camino, F. E., Zhou, W. & Goldman, V. J. Aharonov–Bohm superperiod in a Laughlin quasiparticle interferometer. *Phys. Rev. Lett.* **95**, 246802 (2005).

31. Camino, F. E., Zhou, W. & Goldman, V. J. e/3 Laughlin quasiparticle primary-filling ν = 1/3 interferometer. *Phys. Rev. Lett.* **98**, 076805 (2007).

32. Willett, R. L., Pfeiffer, L. N. & West, K. W. Measurement of filling factor 5/2 quasiparticle interference with observation of charge e/4 and e/2 period oscillations. *Proc. Natl Acad. Sci. USA* **106**, 8853–8858 (2009).

33. Willett, R. L., Nayak, C., Shtengel, K., Pfeiffer, L. N. & West, K. W. Magnetic-field-tuned Aharonov–Bohm oscillations and evidence for non-Abelian anyons at ν = 5/2. *Phys. Rev. Lett.* **111**, 186401 (2013).

34. Laughlin, R. B. Anomalous quantum Hall effect: an incompressible quantum fluid with fractionally charged excitation. *Phys. Rev. Lett.* **50**, 1395–1398 (1983).

35. Jain, J. K. Composite-fermion approach for the fractional quantum Hall effect. *Phys. Rev. Lett.* **63**, 199–202 (1989).

36. de-Picciotto, R. et al. Direct observation of a fractional charge. *Nature* **389**, 162–164 (1997).

37. Goldman, V. J. Resonant tunneling in the quantum Hall regime: measurement of fractional charge. *Science* **267**, 1010–1012 (1995).

38. Goldman, V. J. Resonant tunneling in the quantum Hall regime: measurement of fractional charge. *Surf. Sci.* **361/362**, 1–6 (1995).

39. Girvin, S. M. Particle–hole symmetry in the anomalous quantum Hall effect. *Phys. Rev. B* **29**, 6012–6014 (1984).

40. MacDonald, A. H. Edge states in the fractional-quantum-Hall-effect regime. *Phys. Rev. Lett.* **64**, 220–223 (1990).

41. Chang, A. M. A unified transport theory for the integral and fractional quantum Hall effects: phase boundaries, edge currents, and transmission/reflection probabilities. *Solid State Commun.* **74**, 871–876 (1990).

42. Beenakker, C. W. J. Edge channels for the fractional quantum Hall effect. *Phys. Rev. Lett.* **64**, 216–219 (1990).

43. Meir, Y. Composite edge states in the ν = 2/3 fractional quantum Hall regime. *Phys. Rev. Lett.* **72**, 2624–2627 (1993).

44. Kane, C. L., Fisher, M. P. A. & Polchinski, J. Randomness at the edge: theory of quantum Hall transport at filling ν = 2/3. *Phys. Rev. Lett.* **72**, 4129–4132 (1994).

45. Bid, A., Ofek, N., Heiblum, M., Umansky, V. & Mahalu, D. Shot noise and charge at the 2/3 composite fractional quantum Hall state. *Phys. Rev. Lett.* **103**, 236802 (2009).

46. Sabo, R. et al. Edge reconstruction in fractional quantum Hall states. *Nat. Phys.* **13**, 491–496 (2017).

47. Hu, Z., Rezayi, E. H., Wan, X. & Yang, K. Edge-mode velocities and thermal coherence of quantum Hall interferometers. *Phys. Rev. B* **80**, 235330 (2009).

48. Wan, X., Yang, K. & Rezayi, E. H. Reconstruction of fractional quantum Hall edges. *Phys. Rev. Lett.* **88**, 056802 (2002).

49. Joglekar, Y. N., Nguyen, H. K. & Murthy, G. Edge reconstructions in fractional quantum Hall systems. *Phys. Rev. B* **68**, 035332 (2003).

50. Goldsten, M. & Gefen, Y. Suppression of interference in quantum Hall Mach–Zehnder geometry by upstream neutral modes. *Phys. Rev. Lett.* **117**, 276804 (2016).

51. Park, J., Gefen, Y. & Sim, H. Topological dephasing in the ν = 2/3 fractional quantum Hall regime. *Phys. Rev. B* **92**, 245437 (2015).

52. Inoue, H. et al. Proliferation of neutral modes in fractional quantum Hall states. *Nat. Commun.* **5**, 4067 (2014).

53. Du, R. R., Stormer, H. L., Tsui, D. C., Pfeiffer, L. N. & West, K. W. Experimental evidence for new particles in the fractional quantum Hall effect. *Phys. Rev. Lett.* **70**, 2944–2947 (1993).

Acknowledgements

Author contributions
J.N. and M.J.M. designed the heterostructures and experiments. S.F., S.L. and G.C.G. conducted molecular beam epitaxy growth. J.N. fabricated the devices, performed the measurements and analysed the data with input from M.J.M. H.S. and R.R. performed numerical simulations. J.N. and M.M. wrote the manuscript with input from all authors.

Competing interests
The authors declare no competing interests.

Additional information
Supplementary information is available for this paper at https://doi.org/10.1038/s41567-019-0441-8.

Reprints and permissions information is available at www.nature.com/reprints.

Correspondence and requests for materials should be addressed to M.J.M.

Journal peer review information: *Nature Physics* thanks Thomas Ihn and the other anonymous reviewer(s) for their contribution to the peer review of this work.

Publisher's note: Springer Nature remains neutral with regard to jurisdictional claims in published maps and institutional affiliations.

Methods

The primary quantum well was measured to have a bulk electron density $n = 1.05 \times 10^{11}$ cm^{-2} and mobility $\mu = 7 \times 10^6$ cm^2 V^{-1} s^{-1} measured after full device fabrication and in the dark.

The device was fabricated by: optical lithography and wet etching to define the mesa; deposition of In/Sn Ohmic contacts; electron beam lithography and electron beam evaporation (10 nm Ti/15 nm Au) to define the interferometer gates; optical lithography and electron beam evaporation (20 nm Ti/150 nm Au) to define the bondpads and the surface gates around the Ohmic contacts; mechanical polishing to thin the GaAs substrate; optical lithography and electron beam evaporation (200 nm Ti/150 nm Au) to define the backgates.

The device was measured in a dilution refrigerator with a base mixing chamber temperature $T = 13$ mK. Extensive heat sinking and filtering are used to achieve low electron temperatures and bring the electron temperature close to the cryostat temperature. Standard low-frequency ($f = 13$ Hz) 4-terminal and 2-terminal lock-in amplifier techniques were used to probe the diagonal resistance and conductance across the device. Typically a 200 pA excitation current was used for measurements of integer states and 100 pA excitation was used when measuring fractional states. A +400 mV bias cool was applied to the QPC and side gates while the device was cooled from room temperature; this bias-cool technique results in an approximately 400 mV built-in bias on these gates, which improves device stability.

Data availability

The data that support the plots within this paper and other findings of this study are available from the corresponding author upon reasonable request.